JOURNAL OF ENVIRONMENTAL SCIENCES 41 (2016) 112–120

Available online at www.sciencedirect.com

ScienceDirect

www.elsevier.com/locate/jes

JES JOURNAL OF ENVIRONMENTAL SCIENCES www.jesc.ac.cn

Antimicrobial activity of silver loaded MnO_2 nanomaterials with different crystal phases against *Escherichia coli*

Lian Wang, Hong He, Changbin Zhang, Li Sun, Sijin Liu, Shaoxin Wang*

State Key Joint Laboratory of Environment Simulation and Pollution Control, Research Center for Eco-Environmental Sciences, Chinese Academy of Sciences, Beijing 100085, China

ARTICLE INFO

Article history:
Received 10 February 2015
Revised 10 April 2015
Accepted 17 April 2015
Available online 10 August 2015

Keywords:
Silver
MnO_2
Bactericidal activity
Escherichia coli
ROS

ABSTRACT

Silver-loaded MnO_2 nanomaterials (Ag/MnO_2), including Ag/α-MnO_2, Ag/β-MnO_2, Ag/γ-MnO_2 and Ag/δ-MnO_2 nanorods, were prepared with hydrothermal and impregnation methods. The bactericidal activities of four types of Ag/MnO_2 nanomaterials against *Escherichia coli* were investigated and an inactivation mechanism involving Ag^+ and reactive oxygen species (ROS) was also proposed. The bactericidal activities of Ag/MnO_2 depended on the MnO_2 crystal phase. Among these nanomaterials, Ag/β-MnO_2 showed the highest bactericidal activity. There was a 6-log decrease in *E. coli* survival number after treatment with Ag/β-MnO_2 for 120 min. The results of 5,5-dimethyl-1-pyrroline-N-oxide spin-trapping measurements by electron spin resonance indicate $^{\cdot}OH$ and $^{\cdot}O_2^-$ formation with addition of Ag/β-MnO_2, Ag/γ-MnO_2 or Ag/δ-MnO_2. The strongest peak of $^{\cdot}OH$ appeared for Ag/β-MnO_2, while no $^{\cdot}OH$ or $^{\cdot}O_2^-$ signal was found over Ag/α-MnO_2. Through analysis of electron spin resonance (ESR) and Ag^+ elution results, it could be deduced that the toxicity of Ag^+ eluted from Ag/MnO_2 nanomaterials and ROS played the main roles during the bactericidal process. Silver showed the highest dispersion on the surface of β-MnO_2, which promoted ROS formation and the increase of bactericidal activity. Experimental results also indicated that Ag/MnO_2 induced the production of intracellular ROS and disruption of the cell wall and cell membrane.

Introduction

It is well known that many inorganic antimicrobial agents have been developed, which is very important to providing a sanitary environment and maintain human health. Among these antimicrobial agents, silver has become the most widely used material due to its intrinsic and excellent antimicrobial activity. So far, the antimicrobial mechanism of inorganic antimicrobial agents has mainly involved the toxicity of the metal ions and/or the oxidation role of reactive oxygen species (ROS) (Neal, 2008). ROS have high oxidation ability that could inactivate bacteria quickly, leading to the disruption of cells (Kim et al., 2011; Hwang et al., 2008). Recently, attention has been paid to ROS, such as $^{\cdot}OH$, H_2O_2, and $^{\cdot}O_2^-$, which have high bactericidal efficiency against many kinds of microorganisms (Inoue et al., 2002; Watts et al., 2003; Pape et al., 2004; Jeong et al., 2006; Chang et al., 2008). Generally, photocatalysts such as TiO_2 and ZnO exhibit effective production of ROS when applied in water (Kikuchi et al., 1997; Cho et al., 2004; Hu et al., 2007; Dasari et al., 2013). However, photocatalysis technology requires the use of photon energy and complex devices. Therefore, development of a non-photocatalytic procedure providing abundant formation of ROS is necessary for achieving effective antimicrobial activity. According to the literature, many inorganic bactericidal

* *Corresponding author*. E-mail address: honghe@rcees.ac.cn (Hong He).

http://dx.doi.org/10.1016/j.jes.2015.04.026
1001-0742/

materials such as MgO, CaO, and silver-loaded materials could efficiently inactivate microorganisms through catalytic oxidation processes involving ROS species (Sawai et al., 1997; Inoue et al., 2002; Pape et al., 2004; He et al., 2004; Chen et al., 2007; Chang et al., 2007). Among inorganic bactericidal materials, Ag nanoparticles show high bacterial activity. However, the stability of Ag nanoparticles is poor and stabilizers are used both to control the process of synthesizing Ag nanoparticles and then to prevent their aggregation. Stabilizers usually influence the chemical and biochemical properties (Burkowska-But et al., 2014). Another effective method is to prepare Ag-loaded bacterial materials to improve nanoparticle stability. Further, the interaction of Ag and the support can potentially promote the production of ROS and improve the bactericidal activity.

Our previous studies showed that electron transfer between Ce^{3+}/Ce^{4+}, Ag^{+}/Ag^{0}, and the interaction of Ag and Ce was helpful for the production of ROS (Chang et al., 2008; Wang et al., 2014). In order to examine the universality of this concept, manganese oxides with variable valency were chosen for further research on bactericidal activity based on ROS. Manganese oxides have been considered as unique materials for redox catalysis because of their polyvalent nature, novel chemical and physical properties, low cost and environmentally benign features (Tang et al., 2006a, 2006b; Li et al., 2009). MnO_2 is an excellent catalyst for the oxidation of volatile organic compounds, and much research has been focused on its catalytic properties (Liang et al., 2008; Saputra et al., 2013; Zhang et al., 2015). Further, manganese ions were found to induce Fenton-like reactions for the oxidation of phenol and decolorization of methylene blue (Zhang et al., 2006; Saputra et al., 2013).

MnO_2 can form many kinds of crystal phases such as α-, β-, γ- and δ-MnO_2, with MnO_6 octahedral units linked in different ways (Wang and Li, 2002, 2003). The phase structures can often influence the catalytic activity of MnO_2. Xu et al. (2006) reported that α-MnO_2 nanorods showed higher catalytic activity for CO oxidation than a β-MnO_2 sample. Zhou et al. (2005) reported that nanorods showed higher activity than nanoparticles due to the different numbers of active sites and crystal planes. Recently, the toxic impacts of Mn_2O_3 nanowires on bacteria and cells have been studied (Shamshi Hassan et al., 2012). However, little research has been carried out on the role of ROS and the related bactericidal activity of Ag-loaded MnO_2 nanorods. In this work, α-, β-, γ- and δ-MnO_2 nanorods were prepared via a hydrothermal process. These MnO_2-supported silver (Ag/MnO_2) nanomaterials were tested in this study. The reasons for the different bactericidal activities of Ag/MnO_2 phases were explored. In addition, the formation of ROS was confirmed and a bactericidal mechanism was proposed.

1. Experimental

1.1. Synthesis of Ag/MnO_2 nanorods

α-, β-, γ- and δ-MnO_2 nanomaterials were synthesized by a hydrothermal method according to the literature (Liang et al., 2008). For the preparation of α-MnO_2 nanorods, 1.25 g $KMnO_4$ and 0.525 g $MnSO_4{\cdot}H_2O$ were mixed in 80 mL deionized water and stirred for 30 min. Then, the mixture was transferred into a Teflon-lined stainless steel autoclave (100 mL) and heated at 160°C for 12 hr. The product was washed and dried at 100°C overnight. Similarly, the β-MnO_2 nanorods were obtained from mixture of 1.69 g $MnSO_4{\cdot}H_2O$ and 2.28 g $(NH_4)_2S_2O_8$ hydrothermally heated at 140°C for 12 hr. In the synthesis of γ-MnO_2 nanorods, 3.375 g $MnSO_4{\cdot}H_2O$ and 4.575 g $(NH_4)_2S_2O_8$ were mixed and hydrothermally heated at 90°C for 24 hr. The δ-MnO_2 nanorods were obtained by mixing 1.5 g $KMnO_4$ and 0.275 g $MnSO_4{\cdot}H_2O$ and hydrothermally heating at 240°C for 24 hr.

Ag/MnO_2 samples were prepared by an impregnation method by dispersing an appropriate amount of MnO_2 powder in an aqueous solution of $AgNO_3$. The mixed solution was stirred for 2 hr at room temperature, which was followed by evaporation to dryness in a rotary evaporator at 60°C under reduced pressure. The obtained solid was dried at 100°C overnight and calcined at 550°C for 3 hr in air.

1.2. Characterization

Powder X-ray diffraction (XRD) patterns were obtained on a on an X-ray diffractometer (X'Pert PRO, PANalytical, Japan) using Cu Kα radiation (λ = 0.154 nm) at a scan rate of 6° (2θ)/min, which were used to identify the phase compositions of the samples. Ag/MnO_2 images were obtained using an electron microscope (H-7500, Hitachi, Japan) with operating voltage of 80 kV. Electron spin resonance (ESR) spectra were obtained using an ESR spectrometer (ESP 300E, Bruker, Germany). The settings for the ESR spectrometer were as follows: center field 3480.00 G, microwave frequency 9.75 GHz, and power 20.15 mV. The X-ray absorption near edge structure (XANES) of the Ag K edge was measured in luminescence mode at room temperature on the BL-7C beam line, Photon Factory, Institute of Materials Structure Science, High Energy Accelerator Research Organization (IMSS-KEK, Japan). Ag foil and $AgNO_3$ were used as reference samples. The storage ring was operated at 2.5 GeV with 300 mA as an average storage current. The synchrotron radiation beam line was monochromatized with a Si (111) double crystal monochromator, and mirrors were used to eliminate higher harmonics. The incident and transmitted beam intensities were monitored using ionization chambers filled with pure N_2. XANES data were analyzed using the REX2000 program (RigakuCo., Tsukuba, Japan). X-ray photoelectron spectroscopy (XPS) measurements were performed on a spectrometer (ESCALAB 250Xi, Thermo, USA) using Al Kα radiation (1486.6 eV), with a constant pass energy of 20 eV. The spectra were corrected by referencing C 1 s peaks at 284.8 eV.

1.3. Culture of *Escherichia coli*

E. coli ATCC 8099 was used as the bacterial strain and inoculated into lactose broth (LB) (61748, Fluka Co., Buchs, Switzerland), and cultured aerobically for 24 hr at 37°C with constant agitation. Aliquots of the culture were inoculated into fresh medium and incubated at 37°C for 12 hr until they reached the exponential growth phase. Bacterial cells were collected using centrifugation at 8000 r/min for 10 min, and then the pellet was washed and resuspended with sterilized

water. Finally, bacterial cells were diluted with sterilized water and immediately plated on LB agar plates. The colonies were counted after incubation at 37°C for 24 hr. The cell density corresponding to 10^9–10^{10} colony forming units per milliliter (CFU/mL) was then achieved.

1.4. Test of bactericidal activity

1 mL of *E. coli* suspension was injected into 99 mL of sterilized water, and then the as-prepared Ag/MnO_2 was added to the system. The final nanomaterial concentration was adjusted to an appropriate value, and the final cell concentration was 10^7–10^8 CFU/mL. The reaction mixture was stirred with a magnetic stirrer to prevent settling of the sample. All materials used in the experiments were autoclaved at 121°C for 20 min to ensure sterility. Bacterial suspension without adding nanomaterial was used as a control. At time intervals of 10, 30, 60, and 120 min after addition of Ag/MnO_2, 0.5 mL of bacterial suspension was withdrawn and immediately diluted 10-fold in series with 4.5 mL of 0.9% saline solution and plated on LB agar (61746, Fluka Co., Buchs, Switzerland) plates. Viable cell counts were determined visually as the number of colonies per plate in serial 10-fold dilutions after incubation at 37°C for 24 hr. The reaction temperature was maintained at 25°C. All experiments were carried out in triplicate.

Inhibition zone tests were carried out on solid agar plates partially covered by filter papers with and without Ag/MnO_2. The solid agar plates with a diameter of 90 mm were prepared by mixing nutrient agar and the *E. coli* suspension. The Ag/MnO_2 suspension was dropped on a circle of filter paper with a diameter of 5 mm and dried for 10 min in air. The quantity of Ag/MnO_2 loaded on each filter paper was 1 mg. After the solid agar plates carrying the filter papers were incubated at 37°C for 24 hr, the diameter of the inhibition zone was measured with a vernier caliper to estimate the inhibition properties of Ag/MnO_2.

1.5. Quantitative analysis of silver ions

To carry out quantitative analysis of silver ions eluted from Ag/MnO_2, 5 mL suspension was withdrawn and filtered through a Millipore filter (pore size 0.22 ìm, Millipore, Massachusetts, USA) at each time interval for inductively coupled plasma optical emission spectroscopy (ICP-OES) analysis (Optima 2000, Perkin–Elmer Co., USA). All solutions were prepared with ultrapure water in this experiment. All experiments were repeated three times.

1.6. Reactive oxygen species detection

To determine the production of intracellular ROS, 2′,7′-dichlorofluorescin-diacetate (DCF-DA, Sigma, New Jersey, USA) was used (Su et al., 2009). The *E. coli* samples (1 mL, 10^7 CFU/mL) were collected after centrifugation from LB agar and washed with phosphate-buffered saline (PBS) solution. The *E. coli* samples were then stained with 10 μmol/L DCF-DA for 30 min. After that, *E. coli* samples were treated with Ag/MnO_2 in water. Cells stained with DCF-DA served as the negative control, and H_2O_2 was used as the positive control. Relative fluorescence intensity was recorded using a fluorescent plate reader (Varioskan Flash, Thermo, USA) at an excitation wavelength of 485 nm, and emission was measured at a wavelength of 530 nm. Fluorescence intensity was assayed, which was proportional to intracellular ROS concentration. The formation of highly fluorescent 2′,7′-dichlorofluorescin (DCF) was also estimated with a fluorescent microscope (Zeiss Scope A1, Zeiss, Germany).

1.7. Analysis of structural change

Propidium iodide (PI) was used to examine the disruption of cellular membranes because PI could only influx into cells with disrupted membranes. The staining protocol was as proposed by the manufacturer. *E. coli* (1 mL, 10^7 CFU/mL) were first treated with Ag/MnO_2 (500 mg/L) for 60 min in water and then centrifugated. The substrates were washed with PBS and stained with PI dye (50 g/mL) for 30 min and subsequently analyzed with a fluorescent microscope (Zeiss Scope A1, Zeiss, Germany).

2. Results and discussion

The XRD patterns and TEM (transmission electron microscopy) measurements were used to characterize the various Ag/MnO_2 nanomaterials. From Fig. 1, it can be seen that the XRD patterns exhibit typical α-, β-, γ- and δ-MnO_2 crystal phases (PDF# 44-0141, 24-0735, 14-0644, 80-1098). The intensities and widths of the diffraction peaks of γ- and δ-MnO_2 were greatly lowered and widened compared with those of α- and β-MnO_2. Furthermore, Ag diffraction peaks were not observed in XRD patterns, which indicate that Ag was in an amorphous phase or that the Ag crystalline size was smaller than the detection limit.

Fig. 2 shows TEM images of Ag/MnO_2 samples. The diameters of α-MnO_2 ranged between 30 and 60 nm, and the lengths ranged between 100 and 300 nm. The β-MnO_2 displayed uniform morphologies with diameters of around 60 nm and lengths of 400–600 nm. The widths of γ- and δ-MnO_2 nanorods were 30–40 nm and were narrower than those of α- and β-MnO_2.

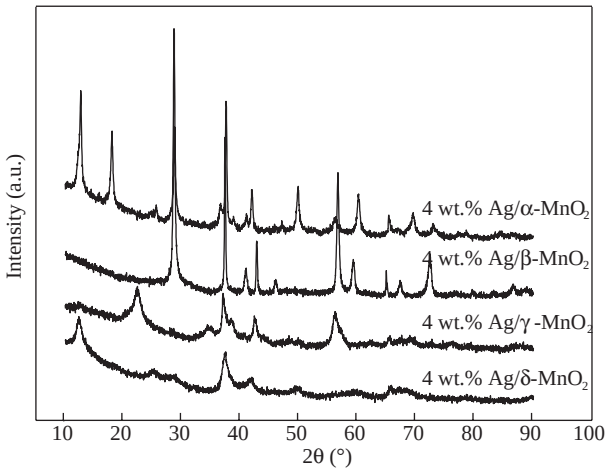

Fig. 1 – X-ray diffraction (XRD) patterns of various Ag/MnO_2 nanomaterials.

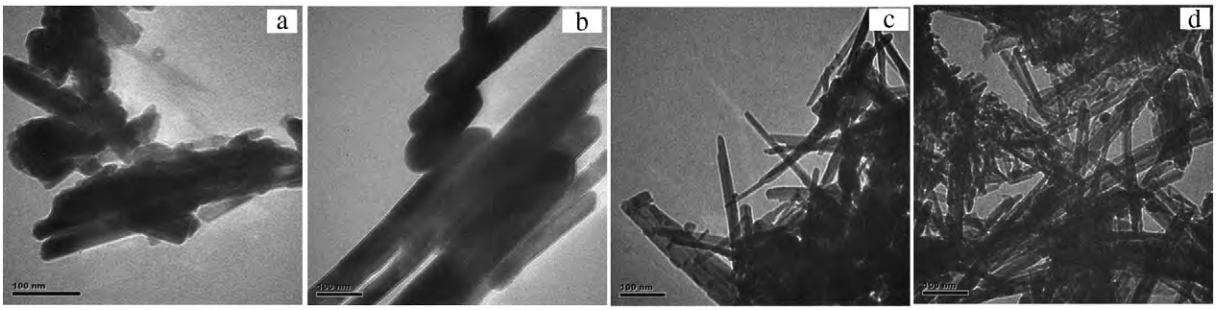

Fig. 2 – Transmission electron microscopy (TEM) photos of (a) 4 wt.% Ag/α-MnO_2, (b) 4 wt.% Ag/β-MnO_2, (c) 4 wt.% Ag/γ-MnO_2, and (d) 4 wt.% Ag/δ-MnO_2.

The bactericidal activities of 2, 4, and 6 wt.% Ag/MnO_2 are shown in Fig. 3a. Among the four types of MnO_2 crystal phases, bactericidal activity varied in the order of Ag/β-MnO_2 > Ag/γ-MnO_2 > Ag/α-MnO_2 ≈ Ag/δ-MnO_2, which might be due to the different surface properties and different interactions between Ag and MnO_2 nanorods. There was a 6-log decrease in *E. coli* survival number after treatment with Ag/β-MnO_2 for 120 min. In general terms, bactericidal activity increased with the increases in silver loading amount and the Ag/MnO_2 concentration (Fig. 3b). Ag/β-MnO_2 showed the highest bactericidal activity regardless of different silver loading amounts and Ag/MnO_2 concentrations.

To test the inhibition activity of Ag/MnO_2, inhibition zone measurement was performed. Fig. 4 shows the images of bacteriological tests performed on solid agar plates partially covered by filter papers with and without Ag/MnO_2. In the case of 4 wt.% Ag/MnO_2, the maximum inhibition zone formed, with a diameter of about 12 mm, indicating that Ag/MnO_2

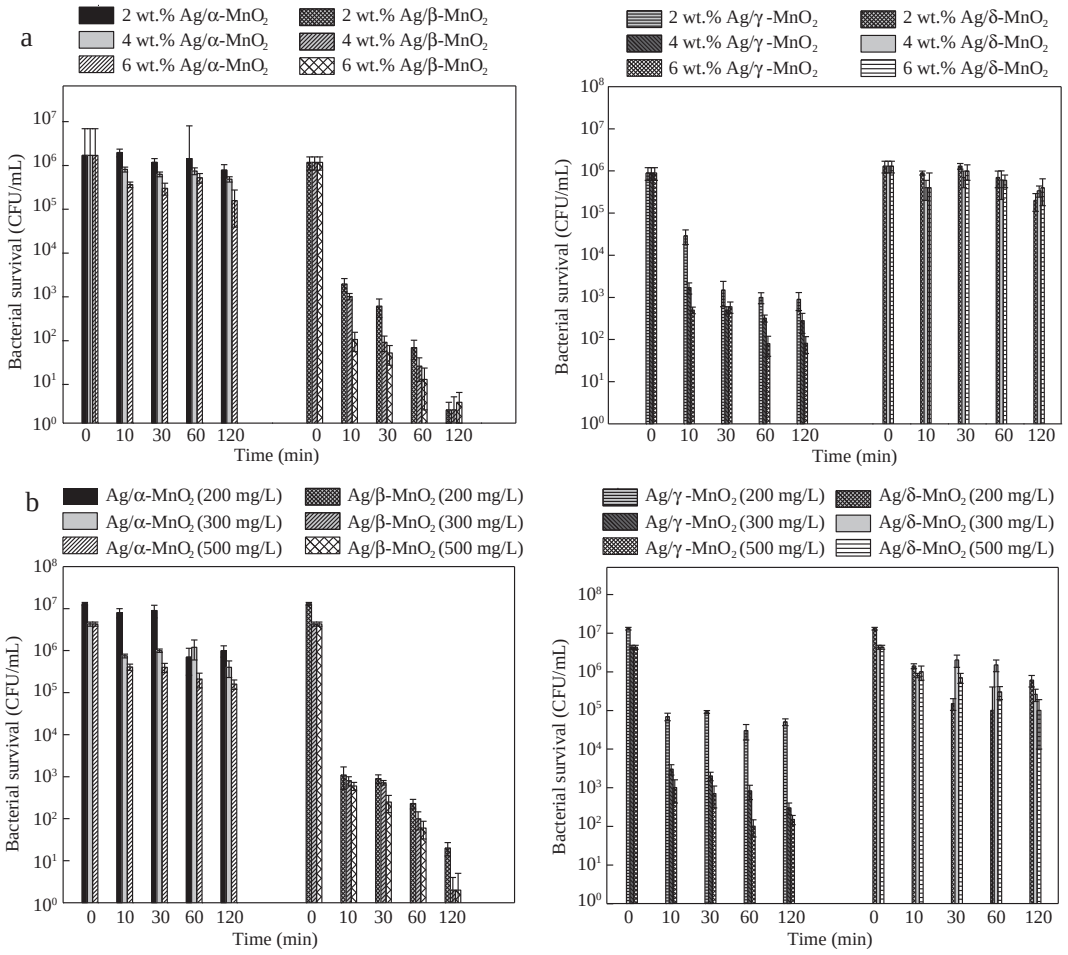

Fig. 3 – Effects of (a) different Ag loading amounts at 300 mg/L Ag/MnO_2 concentration and (b) different Ag/MnO_2 concentrations at 4 wt.% Ag loading against *E. coli* at room temperature. CFU: colony forming units.

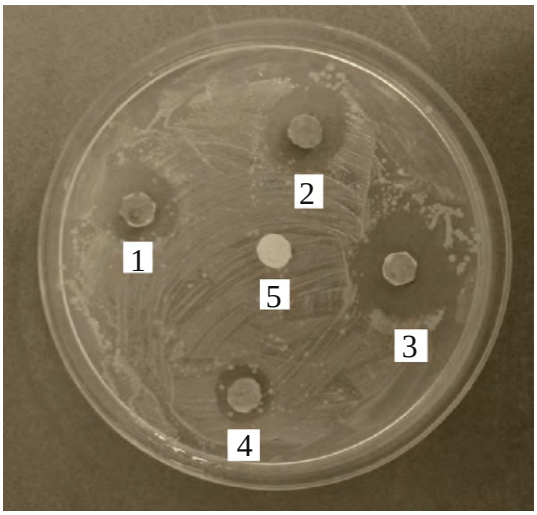

Fig. 4 – Images of *E. coli* incubated for 24 hr at 37°C together with blank filter paper (5#), and filter papers treated with 4 wt.% Ag/α-MnO_2 (1#), 4 wt.% Ag/β-MnO_2 (2#), 4 wt.% Ag/γ-MnO_2 (3#), and 4 wt.% Ag/δ-MnO_2 (4#). Initial bacterial count: 1 × 10^6 CFU.

clearly restrained the proliferation of *E. coli*. By comparison, no inhibition zone appeared around the blank filter paper (5#).

Generally, Ag^+ played an important role in the death of bacteria (Bellinger and Conway, 1970; Feng et al., 2000). The elution of Ag^+ from different Ag/MnO_2 nanomaterials with different silver loading amounts and concentrations was explored. For 2, 4, and 6 wt.% Ag/MnO_2, the order of the eluted Ag^+ concentration was Ag/β-MnO_2 ≈ Ag/γ-MnO_2 ≈ Ag/δ-MnO_2 > Ag/α-MnO_2 (Fig. 5a). For 200, 300, and 500 mg/L Ag/MnO_2, the order of eluted Ag^+ concentration was as follows: Ag/γ-MnO_2 > Ag/δ-MnO_2 > Ag/β-MnO_2 > Ag/α-MnO_2 (Fig. 5b). Ag/α-MnO_2 exhibited the lowest Ag^+ elution concentration, and had the lowest bactericidal activity. The eluted Ag^+ concentration increased with increases in silver loading amount and Ag/MnO_2 concentration. While the eluted Ag^+ concentration did not show a linear increase with increases in silver loading amount and Ag/MnO_2 concentration, it was broadly consistent with the changes in bactericidal activity under different silver loading amounts and Ag/MnO_2 concentrations. Therefore, it could be deduced that Ag^+ played an important role in the bactericidal process. The low and continuous release of silver ions in the bactericidal environment is a critical factor needed to ensure the efficacy of silver ions as an antimicrobial agent (Kwakye-Awuah et al., 2008). Antimicrobial action of silver ion has been reported to

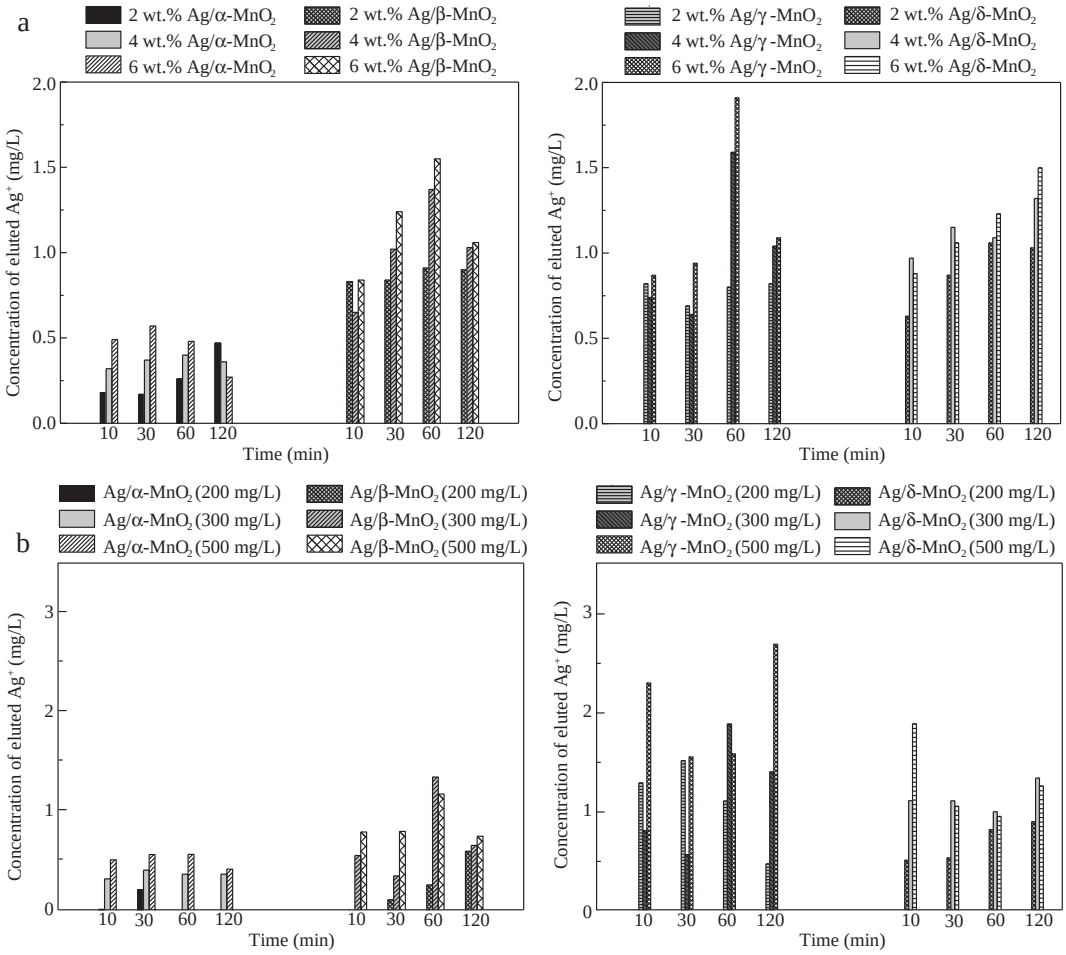

Fig. 5 – Effects of (a) different Ag loading amounts at 300 mg/L Ag/MnO_2 concentration and (b) different Ag/MnO_2 concentrations at 4 wt.% Ag loading on the Ag^+ eluted from Ag/MnO_2.

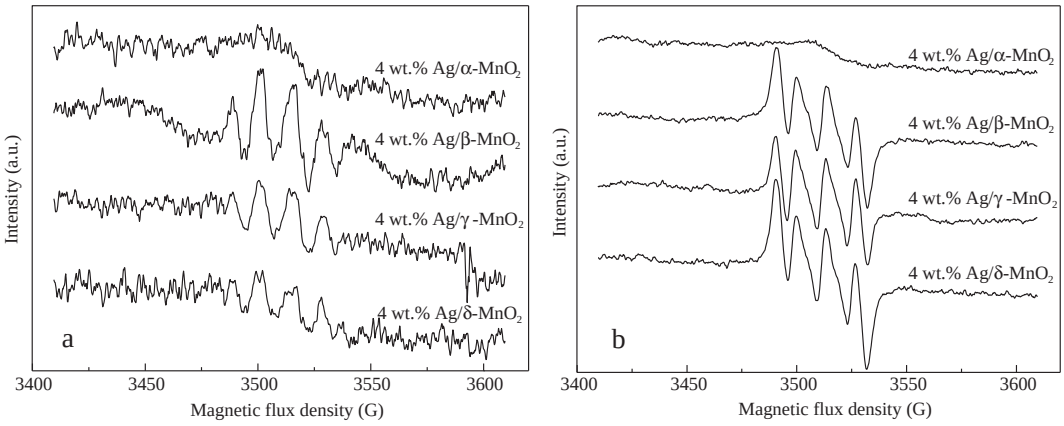

Fig. 6 – 5,5-Dimethyl-1-pyrroline-N-oxide (DMPO) spin-trapping ESR spectra recorded at ambient temperature in (a) aqueous dispersion (for DMPO-$OH^{\cdot}$ adduct) and (b) in methanol dispersion (for DMPO-$O_2^{-\cdot}$ adduct) after the addition of 4 wt.% Ag/MnO_2.

primarily affect the function of membrane-bound enzymes, such as those of the respiratory chain, and the disruption of cell membranes (McDonnell and Russell, 1999; Uchida et al., 2003). However, the eluted Ag^+ concentration was not fully in accord with the bactericidal activity, especially for different crystal phases of Ag/MnO_2. Hence, there might be other impact factors, such as the presence of ROS.

In the bactericidal process, $\cdot OH$ and $\cdot O_2^-$ usually play an important role. In this work, 5,5-dimethyl-1-pyrroline-N-oxide (DMPO) was used as the spin-trapping reagent to determine $\cdot OH$ and $\cdot O_2^-$ radicals. Fig. 6a illustrates the ESR spectra of the DMPO-$OH^{\cdot}$ spin adduct measured immediately after the mixing of the Ag/MnO_2 samples with DMPO solution at room temperature. The four characteristic peaks of the DMPO-$OH^{\cdot}$ species, a 1:2:2:1 quartet pattern, were clearly observed after the addition of Ag/β-MnO_2. Weaker DMPO-$OH^{\cdot}$ signals were also observed for Ag/γ-MnO_2 and Ag/δ-MnO_2. Similarly, the characteristic peaks of DMPO-$O_2^{-\cdot}$ adducts were also observed for Ag/β-MnO_2, Ag/γ-MnO_2 and Ag/δ-MnO_2 in methanol solution after the addition of the samples, as shown in Fig. 6b. However, no ESR signals appeared for Ag/α-MnO_2 samples. These results indicate that ROS were favorable to the catalytic oxidation of *E. coli* cells, since Ag/β-MnO_2 had the highest bactericidal activity and Ag/α-MnO_2 had the lowest bactericidal activity. Thus, direct evidence of $\cdot OH$ and $\cdot O_2^-$ formation on the surface of Ag/MnO_2 provided a strong indication that Ag/MnO_2 effectively activated the adsorbed oxygen to produce active oxygen species, which played important roles in the inactivation of *E. coli*. According to our results of $\cdot OH$ formation on the surface of Ag/CeO_2 (Wang et al., 2014) and Ag/MnO_2 in this study, it can be inferred that multivalent metal oxide supports are favorable to ROS formation.

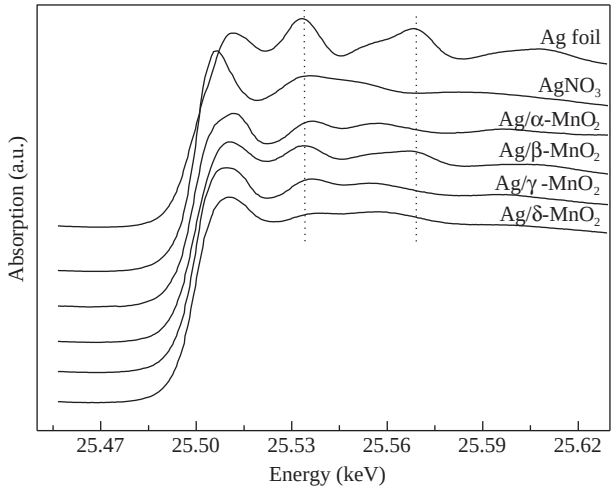

Fig. 7 – XANES (X-ray absorption near edge structure) spectra recorded at the Ag K-edge on 4 wt.% Ag/MnO_2 nanomaterials.

No silver diffraction peak was observed in the XRD patterns. In order to further examine the state of silver on Ag/MnO_2, the XANES spectra of the Ag K-edge were obtained and are shown in Fig. 7. The XANES spectra of 4 wt.% Ag/β-MnO_2 was similar to that of the Ag foil reference, while the XANES spectra of other samples were not similar to that of either Ag foil or $AgNO_3$, which might be due to a mixture of Ag^0 and Ag^+. Thus, the ratio of Ag^0 and Ag^+ was calculated through Ag XANES linear fitting. The fitting data in Table 1 reveal that Ag^0 and Ag^+ co-existed in Ag/MnO_2. The ratio of Ag^0 for 4 wt.% Ag/β-MnO_2 was the highest among the four types of samples. XPS spectra are more surface sensitive than XANES for sample characterization. Fig. 8 shows the XPS spectra of Ag 3d and Mn 2p. As previously reported, the binding energy of the Ag $3d_{5/2}$ peaks of Ag^0 and Ag_2O are located at 368.3 and 367.8 eV, respectively (Tang et al., 2006a, 2006b). Therefore, Ag^0 mainly predominated on the surfaces

Table 1 – Molar ratio of Ag^0 and Ag^+ from XANES linear-fitting results of Ag K-edge and atomic ratio of Ag and Mn from XPS spectra of Ag/MnO_2.

	Molar ratio (%)		Atomic ratio (%)	
	Ag^0	Ag^+	Ag 3d	Mn 2p
4 wt.% Ag/α-MnO_2	40.32	59.68	4.11	95.89
4 wt.% Ag/β-MnO_2	60.92	39.08	17.13	82.87
4 wt.% Ag/γ-MnO_2	30.93	69.07	5.43	94.57
4 wt.% Ag/δ-MnO_2	41.33	58.67	3.64	96.36

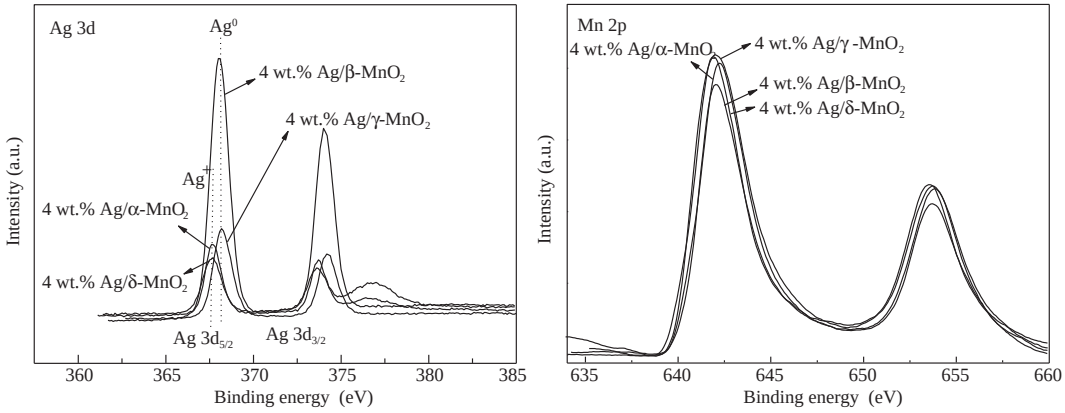

Fig. 8 – XPS (X-ray photoelectron spectroscopy) spectra of Ag 3d and Mn 2p on Ag/MnO_2 nanomaterials.

of Ag/β-MnO_2 and Ag/γ-MnO_2, while Ag^+ was the main species on the surfaces of Ag/α-MnO_2 and Ag/δ-MnO_2. The different detection depths of XPS and XANES led to the different species distribution results observed. XPS spectra of Mn 2p showed a strong peak at 641.9–642.2 eV, mainly attributed to Mn^{4+} and a small amount of Mn^{3+} (Wu et al., 2013). These results indicate that the redox cycling of Ag^+/Ag^0 and Mn^{4+}/Mn^{3+} in certain lattices maintained the catalytic process of ROS formation. For Ag/α-MnO_2, a Mn 2p peak appeared at 642.2 eV, which should be fully attributed to Mn^{4+}. No Mn^{3+} appeared, meaning there were few oxygen defects present, which might lead to the lack of ·OH formation for Ag/α-MnO_2. Interestingly, the ratio of Ag to Mn on the sample surfaces showed significant dependence on the crystal phase of the MnO_2 supports, which implied that Ag dispersion was different on the surfaces of the four types of Ag/MnO_2 (Table 1). The ratio of Ag to Mn on the surface of 4 wt.% Ag/β-MnO_2 was the highest, and the ratio of Ag to Mn on the surface of 4 wt.% Ag/γ-MnO_2 was the second highest. Among the four types of Ag/MnO_2, silver had the highest degree of dispersion on the surface of β-MnO_2, which might be helpful for the formation of ·OH and hence the improvement of bactericidal activity.

To examine the effect of ROS induced by Ag/MnO_2 on *E. coli* cells in vivo, DCF-DA was used as an intracellular ROS-indicator for the Ag/MnO_2-treated cells to measure the generation of intracellular ROS (Su et al., 2009). Fig. 9a1–d1 show that *E. coli* cells became DCF positive after Ag/MnO_2 treatment, indicating that intracellular ROS were generated and participated in the Ag/MnO_2-induced cell death. For comparison, relative fluorescence intensity (i.e. relative ROS level) is presented in Fig. 9e. The cells treated with Ag/β-MnO_2 displayed the highest relative ROS level. The sequence of intracellular ROS amount corresponded to that of bactericidal activity. Intracellular ROS, induced by extracellular ROS and Ag^+, was a candidate mediator for cell apoptosis and death.

The membrane integrity of cells was reflected by the influx of membrane-impermeable fluorescent PI. Fig. 9a2–d2 shows that cells treated with Ag/MnO_2 were PI positive. The order of the number of PI positive cells accorded with the order of bactericidal activity. Thus, the death of cells induced by Ag/

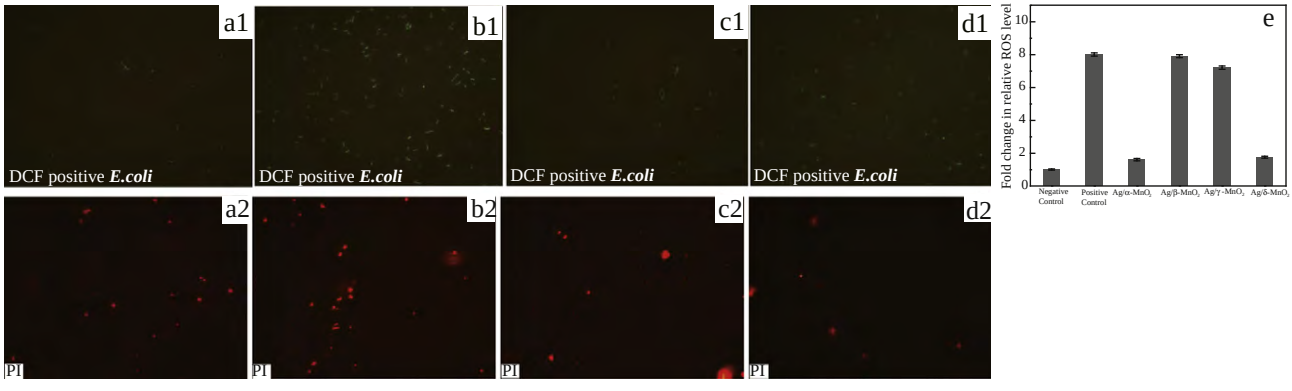

Fig. 9 – Fluorescence microscope photographs of *E. coli* treated with (a) 4 wt.% Ag/α-MnO_2, (b) 4 wt.% Ag/β-MnO_2, (c) 4 wt.% Ag/γ-MnO_2, and (d) 4 wt.% Ag/δ-MnO_2 for 2 hr respectively using 10 μmol/L of 2′,7′-dichlorofluorescin-diacetate (DCF-DA) (1) and propidium iodide (PI, red) (2) as indicators. The average fluorescence intensities using DCF-DA as the indicator (1) are expressed in (e). Sample concentration 500 mg/L and initial bacterial concentration 1 × 10^7 CFU/mL. ROS: reactive oxygen species.

MnO_2 involved the disruption of membrane integrity through the generation of intracellular ROS.

3. Conclusions

In conclusion, Ag/β-MnO_2 possessed the highest bactericidal activity among four crystal phases of Ag/MnO_2 nanomaterials. The bactericidal activities increased with the increase of silver loading amount and nanomaterial concentration. The toxicity of Ag^+ eluted from Ag/MnO_2 provided a major contribution to the bactericidal activities. Furthermore, extracellular $^{\cdot}OH$ and $^{\cdot}O_2^-$ were successfully detected by ESR at room temperature, which provided direct proof for the catalytic inactivation of *E. coli* cells by Ag/MnO_2 catalysts through the activation of molecular oxygen without extra light or electric power input. Silver had the highest dispersion on the surface of Ag/β-MnO_2, which was helpful for the formation of $^{\cdot}OH$ and the increase of bactericidal activity. In all, extracellular ROS and Ag^+ induced the production of intracellular ROS, leading to the disruption of the cell wall and cell membrane, and subsequent cell death.

Acknowledgments

This work was financially supported by the National Natural Science Foundation of China (No. 51208497), the National High Technology Research and Development Program of China (No. 2012AA062702), and International S&T Cooperation Program of China (2013DFM90110).

REFERENCES

Bellinger, C.G., Conway, H., 1970. Effects of silver nitrate and sulfamylon on epithelial regeneration. Plast. Reconstr. Surg. 45 (6), 582–585.

Burkowska-But, A., Sionkowski, G., Walczak, M., 2014. Influence of stabilizers on the antimicrobial properties of silver nanoparticles introduced into natural water. J. Environ. Sci. 26 (3), 542–549.

Chang, Q.Y., Yan, L.Z., Chen, M.X., He, H., Qu, J.H., 2007. Bactericidal mechanism of Ag/Al_2O_3 against *Escherichia coli*. Langmuir 23 (22), 11197–11199.

Chang, Q.Y., He, H., Zhao, J.C., Yang, M., Qu, J.H., 2008. Bactericidal activity of a Ce-promoted Ag/$AlPO_4$ catalyst using molecular oxygen in water. Environ. Sci. Technol. 42 (5), 1699–1704.

Chen, M.X., Yan, L.Z., He, H., Chang, Q.Y., Yu, Y.B., Qu, J.H., 2007. Catalytic sterilization of *Escherichia coli* K 12 on Ag/Al_2O_3 surface. J. Inorg. Biochem. 101 (5), 817–823.

Cho, M., Chung, H., Choi, W., Yoon, J., 2004. Linear correlation between inactivation of *E. coli* and OH radical concentration in TiO_2 photocatalytic disinfection. Water Res. 38 (4), 1069–1077.

Dasari, T.P., Pathakoti, K., Hwang, H.M., 2013. Determination of the mechanism of photoinduced toxicity of selected metal oxide nanoparticles (ZnO, CuO, Co_3O_4 and TiO_2) to *E. coli* bacteria. J. Environ. Sci. 25 (5), 882–888.

Feng, Q.L., Wu, J., Chen, G.Q., Cui, F.Z., Kim, T.N., Kim, J.O., 2000. A mechanistic study of the antibacterial effect of silver ions on *Escherichia coli* and *Staphylococcus aureus*. J. Biomed. Mater. Res. A 52 (4), 662–668.

He, H., Dong, X.P., Yang, M., Yang, Q.X., Duan, S.M., Yu, Y.B., et al., 2004. Catalytic inactivation of SARS coronavirus, *Escherichia coli* and yeast on solid surface. Catal. Commun. 5 (3), 170–172.

Hu, C., Guo, J., Qu, J.H., Hu, X.X., 2007. Photocatalytic degradation of pathogenic bacteria with AgI/TiO_2 under visible light irradiation. Langmuir 23 (9), 4982–4987.

Hwang, E.T., Lee, J.H., Chae, Y.J., Kim, Y.S., Kim, B.C., Sang, B., et al., 2008. Analysis of the toxic mode of action of silver nanoparticles using stress-specific bioluminescent bacteria. Small 4 (6), 746–750.

Inoue, Y., Hoshino, M., Takahashi, H., Noguchi, T., Murata, T., Kanzaki, Y., et al., 2002. Bactericidal activity of Ag–zeolite mediated by reactive oxygen species under aerated conditions. J. Inorg. Biochem. 92 (1), 37–42.

Jeong, J., Kim, J.Y., Yoon, J., 2006. The role of reactive oxygen species in the electrochemical inactivation of microorganisms. Environ. Sci. Technol. 40 (19), 6117–6122.

Kikuchi, Y., Sunada, K., Iyoda, T., Hashimoto, K., Fujishima, A., 1997. Photocatalytic bactericidal effect of TiO_2 thin films: dynamic view of the active oxygen species responsible for the effect. J. Photochem. Photobiol., A 106 (1-3), 51–56.

Kim, S.W., Baek, Y.W., An, Y.J., 2011. Assay-dependent effect of silver nanoparticles to *Escherichia coli* and *Bacillus subtilis*. Appl. Microbiol. Biotechnol. 92 (5), 1045–1052.

Kwakye-Awuah, B., Williams, C., Kenward, M.A., Radecka, I., 2008. Antimicrobial action and efficiency of silver-loaded zeolite X. J. Appl. Microbiol. 104 (5), 1516–1524.

Li, W.B., Wang, J.X., Gong, H., 2009. Catalytic combustion of VOCs on non-noble metal catalysts. Catal. Today 148 (1-2), 81–87.

Liang, S.H., Teng, F., Bulgan, G., Zong, R.L., Zhu, Y.F., 2008. Effect of phase structure of MnO_2 nanorod catalyst on the activity for CO oxidation. J. Phys. Chem. C 112 (14), 5307–5315.

McDonnell, G., Russell, A.D., 1999. Antiseptics and disinfectants: activity, action and resistance. Clin. Microbiol. Rev. 12 (1), 147–179.

Neal, A.L., 2008. What can be inferred from bacterium–nanoparticle interactions about the potential consequences of environmental exposure to nanoparticles? Ecotoxicology 17 (5), 362–371.

Pape, H.L., Solano-Serena, F., Contini, P., Devillers, C., Maftah, A., Leprat, P., 2004. Involvement of reactive oxygen species in the bactericidal activity of activated carbon fibre supporting silver Bactericidal activity of ACF(Ag) mediated by ROS. J. Inorg. Biochem. 98 (6), 1054–1060.

Saputra, E., Muhammad, S., Sun, H.Q., Ang, H.M., Tadé, M.O., Wang, S.B., 2013. Different crystallographic one-dimensional MnO_2 nanomaterials and their superior performance in catalytic phenol degradation. Environ. Sci. Technol. 47 (11), 5882–5887.

Sawai, J., Kojma, H., Ishizu, N., Itoh, M., Igarashi, H., Sawaki, T., et al., 1997. Bactericidal action of magnesium oxide powder. J. Inorg. Biochem. 67 (1-4), 443.

Su, H.L., Chou, C.C., Hung, D.J., Lin, S.H., Pao, I.C., Lin, J.H., et al., 2009. The disruption of bacterial membrane integrity through ROS generation induced by nanohybrids of silver and clay. Biomaterials 30 (30), 5979–5987.

Tang, X.F., Li, Y.G., Huang, X.M., Xu, Y.D., Zhu, H.Q., Wang, J.G., et al., 2006a. MnO_x–CeO_2 mixed oxide catalysts for complete oxidation of formaldehyde: effect of preparation method and calcination temperature. Appl. Catal., B 62 (3-4), 265–273.

Tang, X.F., Chen, J.L., Li, Y.G., Li, Y., Xu, Y.D., Shen, W.J., 2006b. Complete oxidation of formaldehyde over Ag/MnO_x–CeO_2 catalysts. Chem. Eng. J. 118 (1-2), 119–125.

Uchida, M., Yamamoto, T., Taniguchi, A., 2003. Reaction of silver ions and some amino acids. Bokin Bobai 31 (11), 695–704.

Wang, X., Li, Y.D., 2002. Selected-control hydrothermal synthesis of α- and β-MnO_2 single crystal nanowires. J. Am. Chem. Soc. 124 (12), 2880–2881.

Wang, X., Li, Y.D., 2003. Synthesis and formation mechanism of manganese dioxide nanowires/nanorods. Chem. Eur. J. 9 (1), 300–306.

Wang, L., He, H., Yu, Y.B., Sun, L., Liu, S.J., Zhang, C.B., et al., 2014. Morphology-dependent bactericidal activities of Ag/CeO_2 catalysts against *Escherichia coli*. J. Inorg. Biochem. 135, 45–53.

Watts, R.J., Washington, D., Howsawkeng, J., Loge, F.J., Teel, A.L., 2003. Comparative toxicity of hydrogen peroxide, hydroxyl radicals, and superoxide anion to *Escherichia coli*. Adv. Environ. Res. 7 (4), 961–968.

Wu, Y.S., Lu, Y., Song, C.J., Ma, Z.C., Xing, S.T., Gao, Y.Z., 2013. A novel redox-precipitation method for the preparation of α-MnO_2 with a high surface Mn^{4+} concentration and its activity toward complete catalytic oxidation of o-xylene. Catal. Today 201, 32–39.

Xu, R., Wang, X., Wang, D.S., Zhou, K.B., Li, Y.D., 2006. Surface structure effects in nanocrystal MnO_2 and Ag/MnO_2 catalytic oxidation of CO. J. Catal. 237 (2), 426–430.

Zhang, W.X., Yang, Z.H., Wang, X., Zhang, Y.C., Wen, X.G., Yang, S.H., 2006. Large-scale synthesis of β-MnO_2 nanorods and their rapid and efficient catalytic oxidation of methylene blue dye. Catal. Commun. 7 (6), 408–412.

Zhang, J., Zhang, C.B., He, H., 2015. Remarkable promotion effect of trace sulfation on OMS-2 nanorod catalysts for the catalytic combustion of ethanol. J. Environ. Sci. 35, 69–75.

Zhou, K.B., Wang, X., Sun, X.M., Peng, Q., Li, Y.D., 2005. Enhanced catalytic activity of ceria nanorods from well-defined reactive crystal planes. J. Catal. 229 (1), 206–212.